Chemical Science

ROYAL SOCIETY OF CHEMISTRY

EDGE ARTICLE

View Article Online
View Journal

Cite this: DOI: 10.1039/d6sc03342c

All publication charges for this article have been paid for by the Royal Society of Chemistry

Surface-hydrogenation activity regulation toward robust anti-poisoning of ZrCo-based hydrogen isotope storage materials

Qianwen Zhou,[a] Yiting Yu,[a] Panpan Zhou,*[ac] Shunrui Xiao,[a] Jingyu Hu,[a] Xuezhang Xiao,*[ad] Xingwen Feng,[e] Huaqin Kou,*[e] Wenhua Luo,[e] Xiulin Fan*[a] and Lixin Chen*[abf]

The ZrCo alloy is promising for hydrogen isotope storage but suffers from severe CO poisoning due to d-orbital back-donation into CO π^* orbitals, leading to strong chemisorption that blocks subsequent hydrogen dissociation. To address this, we conceptualize a surface-hydrogenation activity factor ($\vec{\eta}$) as a descriptor for screening doping elements. This factor integrates key surface chemical parameters, including local lattice distortion, CO adsorption behavior, and the hydrogen dissociation energy barrier. Guided by η, we designed and synthesized a single-phase $ZrCo_{0.97}V_{0.03}$ alloy. Compared with pristine ZrCo, it exhibits a threefold enhancement in hydrogenation kinetics in a H_2 + CO mixed-gas atmosphere. Mechanistically, V-induced localized tensile strain elevates the surface potential and modulates charge transfer, lowering the H_2 dissociation barrier in the presence of CO. Consequently, the $ZrCo_{0.97}V_{0.03}$ alloy maintains superior hydrogenation kinetics and cycling stability (80.1% retention) after 25 cycles in a mixed gas, validating the η-based design strategy. This work establishes a surface-chemistry-guided approach linking dopant-induced structural modulation to poisoning-tolerant hydrogen storage performance.

Received 22nd April 2026
Accepted 14th May 2026

DOI: 10.1039/d6sc03342c

rsc.li/chemical-science

Introduction

Controlled nuclear fusion is widely recognized as a transformative energy technology for the future, capable of delivering abundant clean energy and serving as a highly promising approach for addressing the global energy crisis.[1–7] Nevertheless, the radioactive nature and high cost of tritium make the safe and efficient storage and supply of deuterium–tritium fuel a critical challenge for the International Thermonuclear Experimental Reactor (ITER).[8,9] Among various hydrogen isotope storage materials, ZrCo alloy is distinguished by its multiple advantages, such as low hydrogenation equilibrium pressure (10^{-3} Pa) at room temperature, low dehydrogenation temperature (350 °C at 1 bar), excellent reaction kinetics, minimal hydrogen isotope effects, and high helium retention capability.[10–12]

However, under the high-energy operating conditions of fusion reactors, deuterium–tritium mixed fuels inevitably contain impurity gases such as Ar, He, CH_4, N_2, CO, CO_2, and O_2,[13–15] which adversely affect the hydrogenation kinetics, saturation capacity, and cycling stability of the material. Among these gases, CO exhibits the most significant poisoning effect on ZrCo alloys,[14,16,17] shown in Fig. S1. According to the Blyholder model, strong chemical interaction exists between CO molecules and the active sites on the substrate surface, primarily due to electron donation from the CO 5σ orbital to the metal d orbital and back-donation of d-electrons to the CO 2π^* antibonding orbital.[18,19] For instance, Prigent *et al.*[20] reported that the hydrogenation capacity of a ZrCo alloy dropped to only 0.21 wt% after 72 h of exposure to a 95% H_2 + 5% CO atmosphere. Therefore, developing effective CO-resistant modifications for ZrCo-based hydrogen isotope storage materials is highly necessary.

Strategies for enhancing the poisoning resistance of hydrogen storage alloys primarily include surface modification and compositional optimization.[21,22] Owing to palladium's excellent hydrogen dissociation capability and strong resistance to impurity gas adsorption, surface coating with a Pd film can effectively improve the poisoning tolerance.[23] However, due to the weak interfacial bonding strength between the Pd coating

[a]State Key Laboratory of Silicon and Advanced Semiconductor Materials, School of Materials Science and Engineering, Zhejiang University, Hangzhou 310058, Zhejiang, China. E-mail: lxchen@zju.edu.cn; xlfan@zju.edu.cn
[b]Institute of Wenzhou, Zhejiang University, Wenzhou 325006, China
[c]College of Materials Science and Engineering, Hohai University, Changzhou 213200, Jiangsu, China. E-mail: ppzhou@hhu.edu.cn
[d]School of Advanced Energy, Sun Yat-sen University (Shenzhen), Shenzhen 518107, Guangdong, China. E-mail: xiaoxzh6@mail.sysu.edu.cn
[e]Institute of Materials, China Academy of Engineering Physics, Mianyang 621907, Sichuan, China. E-mail: kouhuaqin@caep.cn
[f]Key Laboratory of Hydrogen Storage and Transportation Technology of Zhejiang Province, Hangzhou 310027, Zhejiang, China

and the substrate, the Pd film tends to detach from the ZrCo alloy surface during repeated de-/hydrogenation cycles, exposing fresh surfaces and leading to further degradation of anti-poisoning properties.[24,25] In contrast, alloying modification offers a more convenient and stable approach by effectively tuning the bulk and surface electronic structures of the material. Nevertheless, research on the influence of alloying modifications on the poisoning resistance of ZrCo-based alloys remains relatively limited. Zhang *et al.*[26] found that a Ti-substituted $Zr_{0.8}Ti_{0.2}Co$ alloy exhibited even poorer poisoning resistance compared to pristine ZrCo. Depth profiling *via* secondary ion mass spectrometry revealed that Ti promotes the adsorption and dissociation of CO on the surface, resulting in the formation of cobalt carbides and oxides, which in turn hinders the adsorption and dissociation of H_2 as well as the overall hydrogen storage process. Recently, Yao *et al.*[27] reported that B-side substitution of Co with Cr can significantly enhance the poisoning resistance of ZrCo-based alloys. The observed enhancement is ascribed to the chain effect induced by Cr doping, which involves the oxidation resistance and easy hydrogenation of the $ZrCr_2$ phase, the dual sacrificial and catalytic function of *in situ* formed metallic Cr clusters, and the protection offered by Cr oxide layers. However, the presence of multiple phases often poses challenges to the comprehensive hydrogen storage properties. Therefore, developing single-phase ZrCo-based alloys with superior poisoning resistance is highly desirable. Theoretically, strategic alloying substitution can effectively modulate the surface's electronic and defect structures, leading to a subsequent alteration of its adsorption behavior towards CO and its dissociation activity towards hydrogen. However, such investigations remain to be done for hydrogen isotope storage materials.

In this work, we propose a surface-hydrogenation activity factor (η) as a qualitative evaluation indicator. This indicator guided our systematic investigation into how heteroatom doping modulates the local lattice strain and d-orbital electron shift of the ZrCo alloy surface, and the consequent alterations in CO adsorption behavior and hydrogen dissociation driving force. Based on these design principles, we successfully developed and validated a micro-alloying strategy using V, leading to the synthesis of a single-phase $ZrCo_{0.97}V_{0.03}$ alloy. Compared to the pristine ZrCo alloy, the optimized material exhibits a 3-fold enhancement in hydrogenation kinetics under a H_2 + 5000 ppm CO atmosphere, along with favorable cycling durability. The micro-alloying strategy proposed in this study offers a convenient route to significantly improve the poisoning resistance of ZrCo alloys while preserving their intrinsic hydrogen storage characteristics. This study provides a clear design strategy for developing poisoning-resistant hydrogen storage materials.

Results and discussion

Rational selection of doping element

Due to the poisoning effects of impurity gases on metal hydrides, CO preferential adsorbs on the active sites, which inhibits the hydrogen adsorption and dissociation process. Accordingly, the resulting sluggish hydrogenation kinetics has become a major bottleneck for practical application (Fig. 1(a)). To identify the optimal alloying element for enhanced anti-poisoning resistance of ZrCo-based alloys, this study proposed a surface-hydrogenation activity factor ($\vec{\eta}$) as a qualitative evaluation indicator (Fig. 1(b)). According to the principles of hydrogen storage, different elements exhibit selective substitution preferences for the lattice sites. Elements such as Ti, Nb, and Hf tend to substitute on the Zr side, while Fe, Ni, and Cu preferentially occupy the Co side, thereby influencing the hydrogen dissociation capability.[28] Meanwhile, the lattice expansion or contraction induced by elemental substitution can trigger local lattice strain, which in turn modulates the surface activity of the alloy.

The vector $\vec{\eta}$ is collectively determined by both the surface activity and hydrogenation activity, which is defined by $\vec{\eta} = (\Delta E_H, \varepsilon)$. Here, ΔE_H = (HSDE(M) − HSDE(ZC))/HSDE(ZC) (M is the substituted alloy, and ZC is the original ZrCo alloy) represents the difference in hydrogen spontaneous dissociation energy (HSDE) on the doped surface *versus* the ZrCo surface, while $\varepsilon = (a(M) - a(ZC))/a(ZC)$ denotes the relative change in lattice parameter a induced by doping. Both quantities are obtained from DFT calculations. Since both ΔE_H and ε can be positive or negative, and a positive value for each is considered most favorable for improving poisoning resistance, we treat ΔE_H and ε as the y- and x-components of $\vec{\eta}$, respectively. The magnitude and direction of $\vec{\eta}$ are then determined *via* vector addition, preserving the signs of both components.

Based on this definition, $\vec{\eta}$ quantifies the synergistic effect of elemental substitution on both surface activity and hydrogen dissociation capability. Due to the atomic size mismatch between dopant and host elements, doping typically introduces lattice strain, as shown in Fig. 1(c–e) and S3. Substituting host atoms with a larger atomic radius induces lattice expansion, resulting in tensile strain. Lattice strain is generally defined as the deviation of interatomic distances from their equilibrium positions, which can be quantified by the normalized ratio of the change in lattice parameters to their unstrained original values.[29,30] As the strain shifts from negative to positive, the d band center of Co on the ZrCo (110) surface moves upward toward the Fermi level (Fig. 1(d)), thereby elevating the overall surface activity of the alloy. This shift is schematically illustrated in Fig. 1(e), where the upward movement of the d band center towards the Fermi level enhances the occupancy of anti-bonding states. Consequently, the interaction between the alloy surface and adsorbates is strengthened, leading to improved catalytic activity.

Following this mechanistic understanding, we systematically calculated the strain induced by various elemental substitutions (Fig. 1(f)) and the corresponding spontaneous hydrogen dissociation energies (Fig. 1(g)). During the alloying screening process, elemental substitutions on the Zr-side and Co-side were considered separately, with candidate elements selected from the third and fourth periods. Based on previous research,[31–33] the Zr-side acts as the hydrogen-absorbing element, with candidates including Sc, Ti, Nb, and Hf; the Co side acts as the hydrogen-dissociating element, with candidates including V, Cr, Mn, Fe, Ni, Cu, Mo, and Pd. The specific

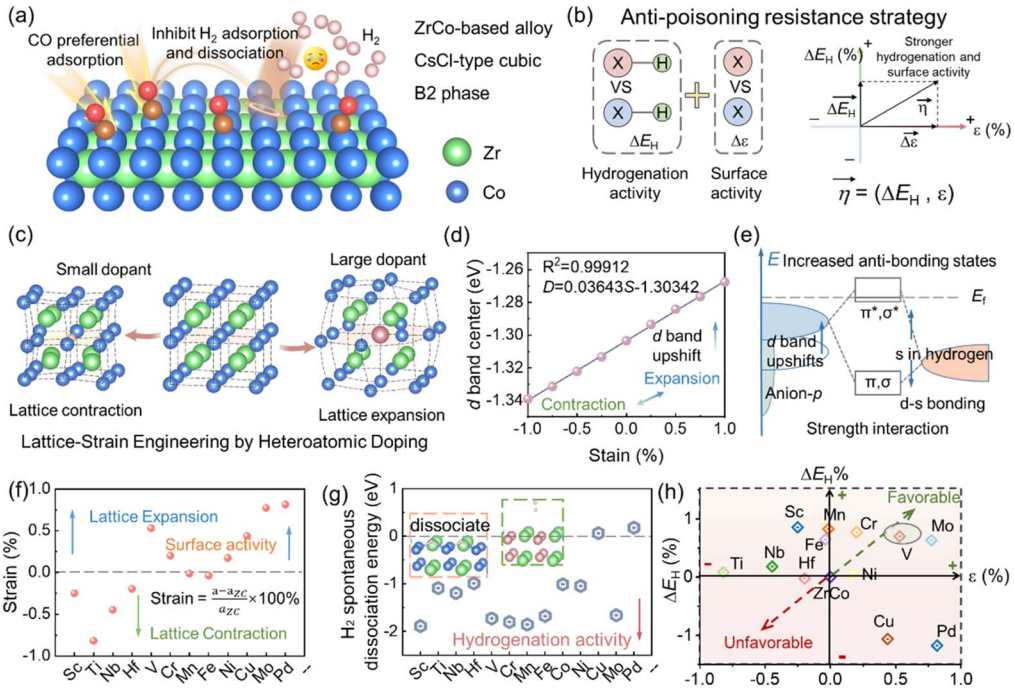

Fig. 1 (a) Schematic illustration of poisoning effects induced by impurity gases. (b) Proposed anti-poisoning strategy of hydrogenation-surface activity factor (η) for ZrCo-based alloy. (c) Schematic illustration of lattice strain induced by heteroatom doping. (d) Modulation of the d-band center of the ZrCo (110) surface by lattice strain. (e) Diagram of bonding orbital energy levels between the H and surface Co atom. (f) Correlation between elemental substitution and induced lattice strain. (g) H_2 spontaneous dissociation energy of the dopant element, and (h) a comprehensive comparision of surface hydrogenation activity.

positions of the dopant atoms are shown in Fig. S4. A comprehensive comparison is shown in Fig. 1(h). Among these candidates, V was identified as the most promising dopant due to its dual functionality. On the one hand, its large atomic radius relative to Co induces tensile strain and enhances surface activity. On the other hand, its intrinsic electronic structure facilitates fluent hydrogen dissociation. This synergy theoretically contributes to superior resistance to CO poisoning. Furthermore, the melting point of V (1910 °C) is only slightly higher than that of Zr (1855 °C). This suitable melting point ensures good processability when V is used to substitute and form the ZrCo-based alloy. To validate the proposed screening method based on the surface-hydrogenation activity factor, Cu, which exhibits poor hydrogen dissociation activity, and Ti, which shows poor surface activity, were also selected as comparative samples for experimental validation (Fig. S5). The experimental results indicate that the incorporation of both of the two alloying elements (Cu & Ti) adversely affects the performance.

Phase structure and transition mechanism

Guided by the selection rationale from the surface hydrogenation activity factor, Zr–Co–(V)-based alloys were prepared by induction levitation melting in a water-cooled copper crucible under an argon atmosphere. The resulting ingots were subsequently activated under 40 bar H_2 for 12 h, as illustrated in Fig. 2(a). The activated ZrCo-based alloy is a black powder with an average particle size of 20 μm (Fig. 2(b)). The XRD patterns of $ZrCo_{1-x}V_x$ (x = 0, 0.01, 0.03, 0.05, 0.1) (named as ZC, $B_{0.01}$, $B_{0.03}$, $B_{0.05}$, $B_{0.1}$) and $Zr_{0.9}V_{0.1}Co$ (named as $A_{0.1}$) alloys at dehydrogenation and hydrogenation states, along with the phase abundances obtained by Rietveld refinement, are shown in Fig. 2(c–g), S6 and S7. Generally, these ZrCo-based alloys at the dehydrogenation state exhibit B2 structure as the main phase, and transition into B33 structure after hydrogenation saturation (Fig. S7). Specifically, when V element substitutes for the Co side at amounts of 0.01 and 0.03, the resulting alloys ($ZrCo_{0.99}V_{0.01}$ and $ZrCo_{0.97}V_{0.03}$) maintain a single-phase B2 structure. The expansion of the lattice parameters correlates with increasing V content, confirming the effective substitution by the larger V atoms. During the solidification of the melt into an ingot, a small amount of V atoms acts as preferential nucleation sites. This promotes the nucleation and crystallization of the ZrCo phase, thereby effectively suppressing the precipitation of $ZrCo_2$. With increasing V substitution, $Zr(Co,V)_2$ precipitates progressively form in the ZrCo-based alloy. Notably, the identity of the secondary phases exhibits a pronounced divergence depending on the substitution side (Zr/Co). The $ZrCo_{0.9}V_{0.1}$ alloy yields a mixture of C14-type $Zr(Co,V)_2$ and Zr_2Co secondary phase, while the $Zr_{0.9}V_{0.1}Co$ alloy leads exclusively to a C15-type $Zr(Co,V)_2$ secondary phase. This distinct site preference indicates that V tends to substitute for Co sites. To further investigate the influence of V element substitution on the structural transition, we performed theoretical calculations to determine the energy difference between the C14- and C15-type Laves-structured $ZrCo_2$ with varying V substitution content. As

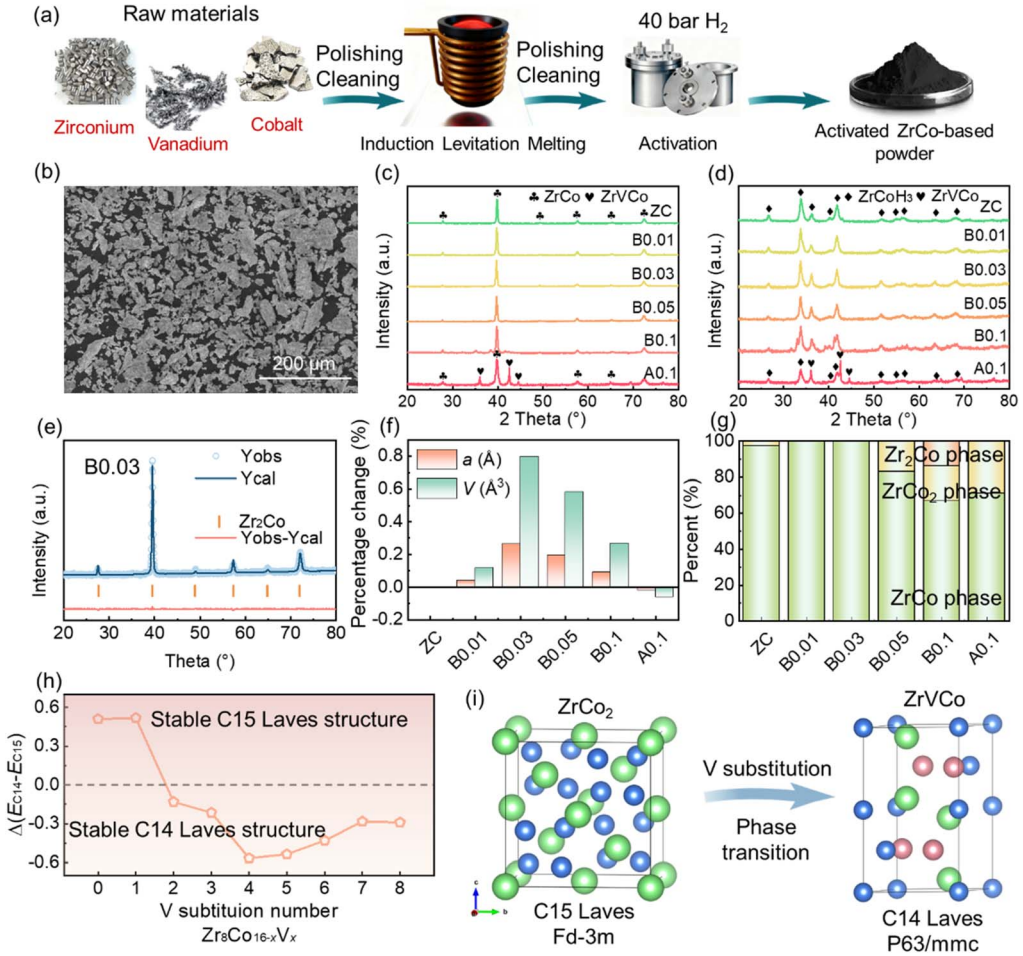

Fig. 2 (a) Schematic illustration of the preparation process of ZrCo-based hydrogen isotope storage alloy. (b) SEM image of activated ZrCo-based powder. XRD patterns of $ZrCo_{1-x}V_x$ (x = 0, 0.01, 0.03, 0.05, 0.1) and $Zr_{0.9}V_{0.1}Co$ alloys at (c) the dehydrogenation state and (d) hydrogenation state. (e) Rietveld refinement result of single-phase $ZrCo_{0.97}V_{0.03}$ alloy. (f) Normalized lattice parameters (relative to pristine ZrCo) and (g) phase abundance for different substitution contents. (h) The energy difference of C15- and C14-type $ZrCo_2$ structure for varying V content. (i) Schematic illustration of V-induced phase transition.

presented in Fig. 2(h–i), the C15-type $ZrCo_2$ exhibits a lower energy than its C14 counterpart, suggesting a more stable crystal structure. With increasing V substitution, the energy difference between the C14- and C15-type Laves-structured $ZrCo_2$ progressively decreases. Once the value becomes negative, a structural transition from C14 to C15 is energetically driven, which is consistent with our experimental observations.[34] SEM and EDS were performed on the $ZrCo_{1-x}V_x$ (x = 0, 0.01, 0.03, 0.05, 0.1) and $Zr_{0.9}V_{0.1}Co$ alloys particles (Fig. S8). The elemental mappings demonstrate a homogeneous distribution of Zr, Co, and V. At higher substitution contents, V-enriched regions become evident, consistent with the precipitation of the secondary phases identified above.

Anti-poisoning behaviours

Subsequently, the hydrogen storage properties of $ZrCo_{1-x}V_x$ (x = 0, 0.01, 0.03, 0.05, 0.1) and $Zr_{0.9}V_{0.1}Co$ alloys were systematically investigated. As shown in Fig. 3(a), the pristine ZrCo alloy shows fast hydrogenation kinetics in the pure hydrogen atmosphere. In contrast, CO poisoning introduces a significantly higher energy barrier, resulting in sluggish kinetics and degraded storage capacity. Hydrogenation kinetic curves in 4 bar pure H_2 and a H_2 + 5000 ppm CO mixture are shown in Fig. 3(b and c). The corresponding saturated hydrogen capacities and T_{90} values, the time required to reach 90% of the saturated capacity in the impurity gas, are summarized in Fig. 3(d).

The hydrogenation curves in pure H_2 demonstrate excellent kinetics, reaching saturation within 100 s. In the single-phase alloys, V substitution slightly enhances the hydrogen saturation capacity, an effect that arises from the stronger hydrogen affinity of V compared to Co. However, when the V element substitution exceeds 0.05, the formation of secondary phases leads to a reduction in capacity. The hydrogen capacity of $ZrCo_{0.9}V_{0.1}$ is 1.92 wt%, while that of $Zr_{0.9}V_{0.1}Co$ is only 1.57 wt%, significantly lower than that of the pristine ZrCo alloy. It is noteworthy that XRD analysis confirms the formation of a C15-type $Zr(Co,V)_2$ secondary phase for the $Zr_{0.9}V_{0.1}Co$ alloy.

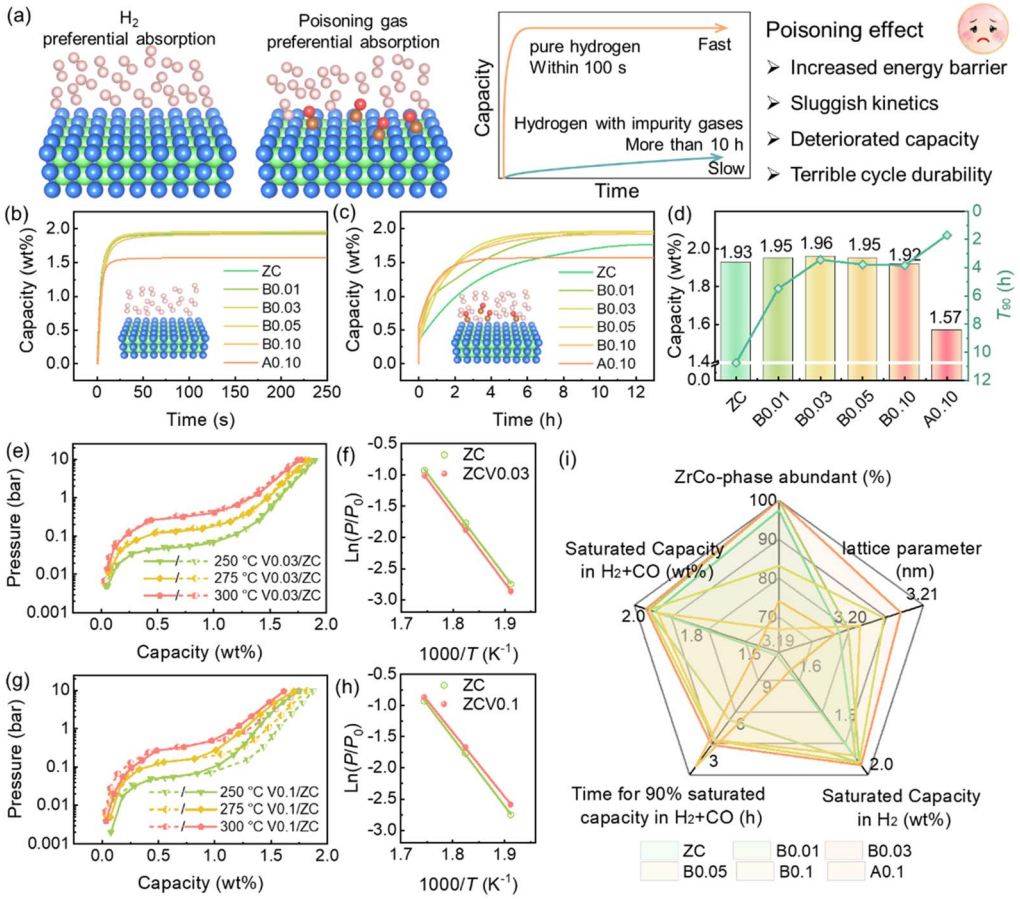

Fig. 3 (a) Illustration diagram of the poisoning effect on ZrCo alloy. Hydrogenation kinetic curves at 4 bar (b) pure H_2, (c) H_2 + 5000 ppm CO, and (d) its corresponding hydrogen capacity and T_{90} (the time of achieving 90% saturated capacity in impurity gas) of $ZrCo_{1-x}V_x$ (x = 0, 0.01, 0.03, 0.05, 0.1) and $Zr_{0.9}V_{0.1}Co$ alloys. Hydrogenation PCT curves of (e) $ZrCo_{0.9}V_{0.1}$ and ZrCo, and (g) $ZrCo_{0.9}V_{0.1}$ and ZrCo at different temperatures and corresponding hydrogenation Van't Hoff plots of (f) $ZrCo_{0.9}V_{0.1}$ and ZrCo, and (h) $ZrCo_{0.9}V_{0.1}$ and ZrCo. (i) Comprehensive comparison of hydrogen storage properties of $ZrCo_{1-x}V_x$ (x = 0, 0.01, 0.03, 0.05, 0.1) and $Zr_{0.9}V_{0.1}Co$ alloys.

Since the C15-type $ZrCo_2$ alloy requires an extreme hydrogen pressure of over 1 GPa for activation and exhibits 0.14 wt% at 60 bar,[35] it contributes minimally to hydrogen uptake under the testing condition of 4 bar. Consequently, its formation is directly responsible for the significant reduction in the overall hydrogen storage capacity.

Notably, the hydrogenation kinetics curves under 4 bar 5000 ppm CO + H_2 were slower than those in pure H_2. V substitution markedly enhances the CO poisoning resistance of the ZrCo-based alloy. Specifically, in a 4 bar mixed gas containing H_2 + 5000 ppm CO, the V-modified ZrCo-based alloy reaches 90% of its saturated hydrogen storage capacity within 3.5 h, substantially faster than the 10.8 h required for pristine ZrCo. However, further increasing the V content does not result in additional improvements in poisoning resistance. This performance plateau is attributed to the limited solid solubility of V within the ZrCo matrix. Excess V precipitates as secondary phases, thereby preventing further lattice expansion and prevents additional enhancement of the hydrogenation reactivity. The hydrogenation kinetics of a material are governed by its thermodynamic plateau pressure. Under identical hydrogenation conditions, a lower plateau pressure corresponds to a greater driving force for the hydrogenation reaction, resulting in faster kinetics. To rule out alterations in the reaction driving force caused by thermodynamic factors, we subsequently conducted pressure–composition–temperature (PCT) measurements (Fig. 3(e–h)). The PCT curve of the micro-V substituted $ZrCo_{0.97}V_{0.03}$ alloy shows a slightly lower plateau pressure, indicating that the small amount of solid-solubilized V effectively enhances the hydrogen binding affinity. In contrast, compared with pristine ZrCo, the $ZrCo_{0.9}V_{0.1}$ alloy exhibits a lower α-phase region and a higher β-phase region in its hydrogenation PCT curve. The lower α-phase region can be attributed to the Zr_2Co secondary phase, which has a lower hydrogen plateau pressure (Zr_2Co: $\sim10^{-6}$ Pa; ZrCo: $\sim10^{-3}$ Pa), while the higher β-phase region results from the C14-type $Zr(V,Co)_2$ phase with a higher plateau pressure. Subsequently, the van't Hoff equation was employed to calculate the thermodynamic parameters, which are listed in Table S1. For pristine ZrCo, the hydrogen absorption enthalpy ΔH is −90.76 kJ per mol H_2, while for the $ZrCo0_{.97}V_{0.03}$ alloy it is −92.28 kJ per mol H_2. The more negative ΔH of the V-substituted alloy indicates

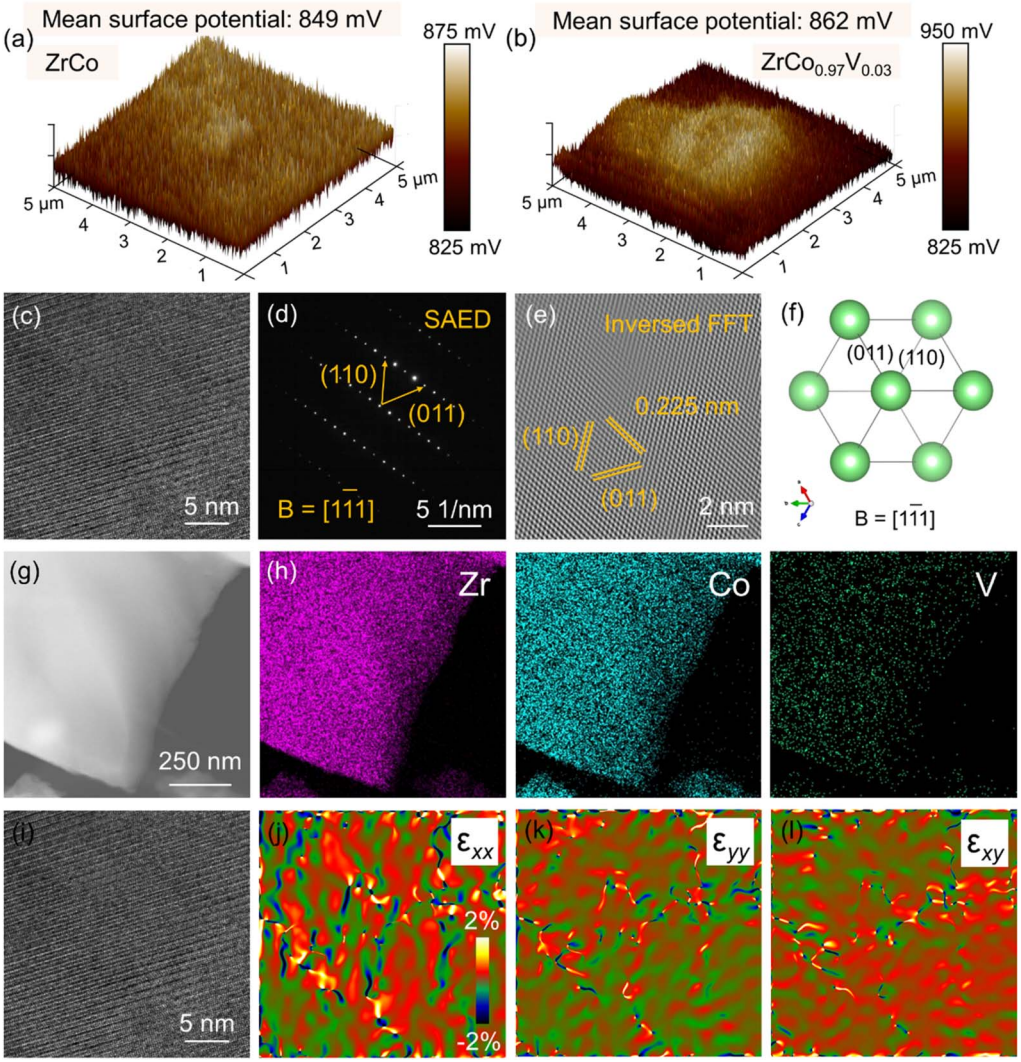

Fig. 4 The KPFM images of (a) ZrCo and (b) $ZrCo_{0.97}V_{0.03}$ alloy. (c) High resolution TEM (HRTEM) image, (d) selected area electron diffraction (SAED) image, (e) inversed fast Fourier transform (FFT), (f) simulated corresponding crystallographic zone axis, (g and h) EDS mapping and (i–l) strain distributions in the $x(\varepsilon_{xx})$, $y(\varepsilon_{yy})$ and $xy(\varepsilon_{xy})$ directions of $ZrCo_{0.97}V_{0.03}$ alloy.

a stronger hydrogen binding affinity, which accounts for its slightly lower plateau pressure and the faster hydrogenation kinetics observed in the CO-containing atmosphere (Fig. 3(c)).

A comprehensive analysis of phase purity, anti-poisoning kinetics, hydrogen capacity, and cost is presented in Fig. 3(i). Among all candidates, the $ZrCo_{0.97}V_{0.03}$ alloy exhibits a single-phase B2 structure and a slightly increased saturation capacity (1.95 wt%) compared to pristine ZrCo (1.93 wt%). Furthermore, its T_{90} value decreases dramatically from 10.8 h (pristine ZrCo) to approximately 3.5 h. Given the performance advantages combined with good cost-effectiveness, the $ZrCo_{0.97}V_{0.03}$ alloy was selected as the preferred composition for further investigation of its cycling performance.

Anti-poisoning mechanism analysis

To further probe the surface characteristics, ZrCo and $ZrCo_{0.97}V_{0.03}$ alloys were characterized using Kelvin probe force microscopy (KPFM) (Fig. 4(a and b)). Specifically, the $ZrCo_{0.97}V_{0.03}$ alloy exhibits a higher surface potential (862 mV) compared to that of the ZrCo alloy (849 mV), implying enhanced surface charge transfer and greater surface activity. The lower electronegativity of V (1.63) relative to Co (1.88) suggests that V has a greater propensity for electron loss. Therefore, substituting Co with V effectively promotes surface charge transfer. Furthermore, we characterized the microstructure of the optimal sample using high resolution TEM (HRTEM) and selected area electron diffraction (SAED), as shown in Fig. 4(c–f).

Distinct spots corresponding to the (110) and (011) planes of the B2 phase were observed along the [111] zone axis. It is worth noting that, due to the relatively large sample thickness, the diffraction pattern exhibited polycrystalline diffraction rings with four periods.[36,37] To accurately measure the crystal plane spacing, we performed an inversed FFT. The resulting IFFT image revealed a measured crystal plane spacing of 0.225 nm (110), consistent with the theoretical value. Additionally, EDS mapping of the ZrCoV alloy confirmed its homogeneous

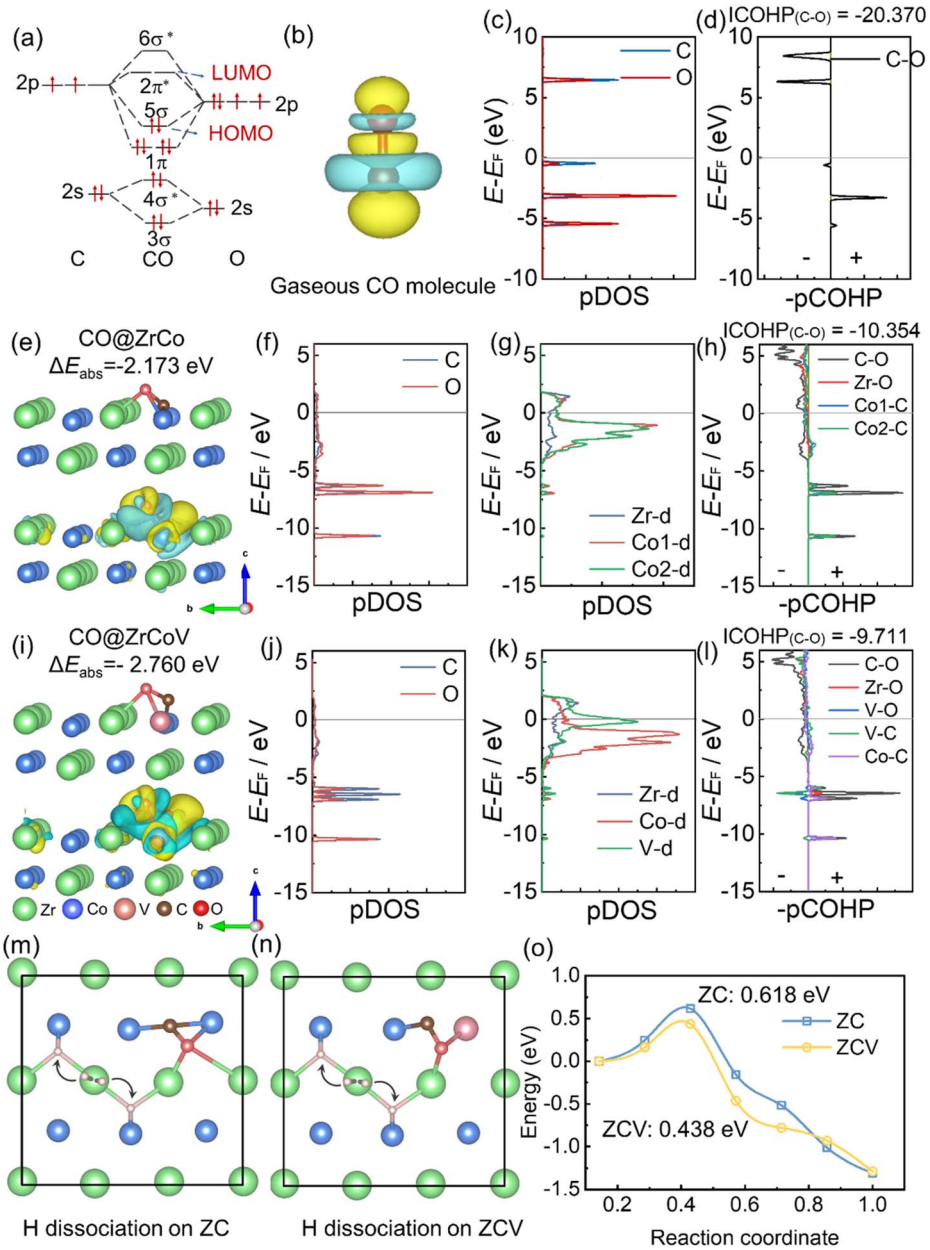

Fig. 5 (a) Molecular orbital, (b) atomic charge difference, and corresponding (c) pDOS and (d) COHP analysis results for the CO gas molecule. Adsorption configurations and set charge difference (isosurface level 0.005) of the CO molecule on (e) ZrCo and (i) B-side Co-substituted ZrCoV, along with the corresponding (f, g, j and k) pDOS and (h and l) COHP analysis results. (m and n) Hydrogen dissociation path on CO@ZrCo and CO@ZrCoV surfaces and (o) corresponding hydrogen dissociation energy barrier.

elemental distribution, demonstrating the accuracy of our preparation *via* levitation melting (Fig. 4(g and h)). To investigate the effect of V substitution on lattice strain, we conducted geometric phase analysis (GPA) on the $ZrCo_{0.97}V_{0.03}$ alloy. As shown in Fig. 4(i–l), the in-plane strain distribution maps obtained *via* GPA from the HRTEM image of the same region are presented sequentially as *x*-axis strain (ε_{xx}), *y*-axis strain (ε_{yy}) and shear strain (ε_{xy}). The color scale is set to $\pm$ 2%, with green indicating negligible strain and red/blue representing tensile/compressive strain, respectively. A pronounced tensile strain (red regions) along the *x*-axis is clearly observed, aligning with the design strategy (Fig. 1). Thus, the introduction of such tensile strain can effectively shift the d-band center toward the Fermi level, thereby further enhancing the surface activity.

To elucidate the mechanism behind the enhanced anti-poisoning properties achieved by V-for-Co substitution, we performed systematic theoretical calculations. To this end, the most stable adsorption configurations were identified. Subsequent analysis included the density of states (DOS) and the C–O bonding strength in both gaseous CO and the absorbed CO@ZrCo and CO@ZrCoV systems.

As shown in Fig. 5(a–d) and Table S2, the integrated crystal orbital Hamiltonian population (ICOHP) at the Fermi level for the gaseous CO molecule is −20.370. The CO reaches its most

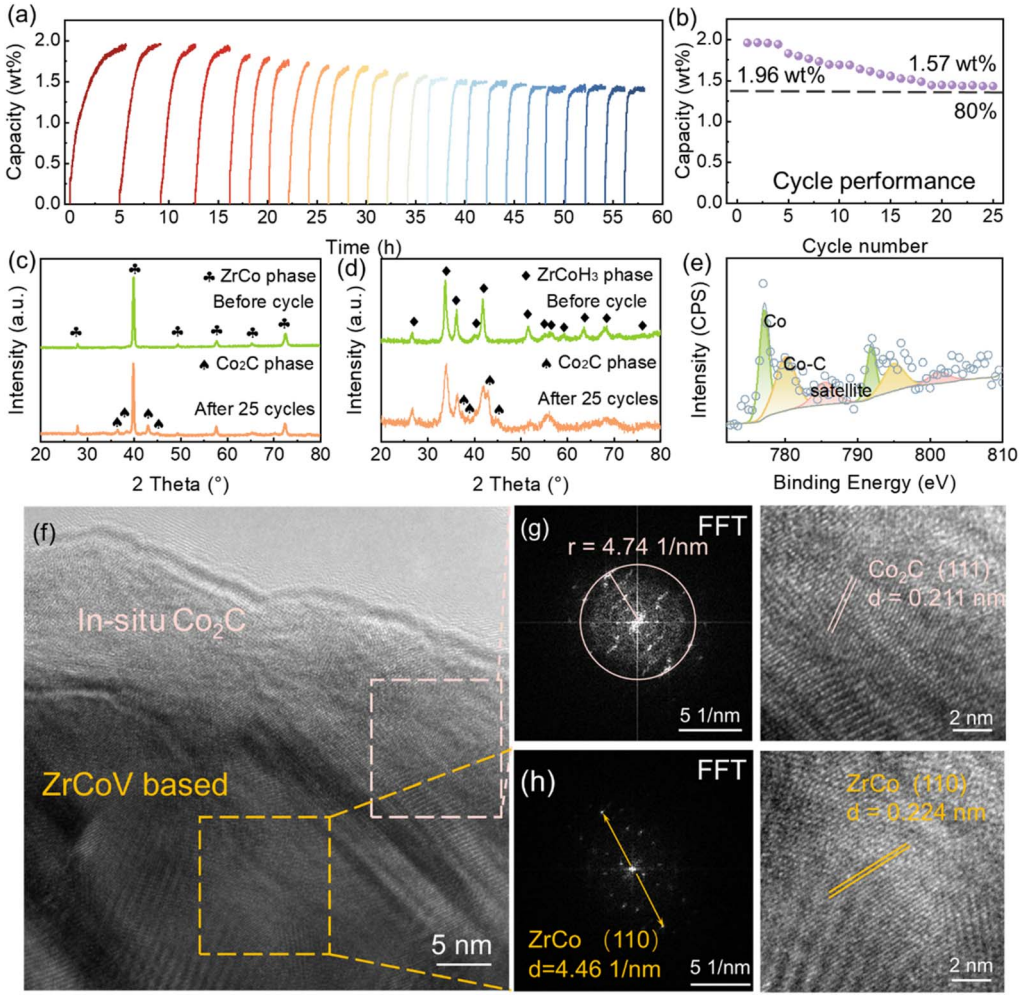

Fig. 6 (a) Cycling performance and (b) corresponding capacity of $ZrCo_{0.97}V_{0.03}$ alloy evaluated using dehydrogenation at 550 °C under dynamic vacuum and re-hydrogenation at 4 bar H_2 + 5000 ppm CO. XRD pattern of $ZrCo_{0.97}V_{0.03}$ alloy before and after cycling at (c) dehydrogenation and (d) hydrogenation states. (e) Co 2p XPS spectra of $ZrCo_{0.97}V_{0.03}$ alloy after cycling in H_2 + 5000 ppm CO. (f) HRTEM image of $ZrCo_{0.97}V_{0.03}$ after cycling, and (g) corresponding FFT of the surface pattern and (h) inner pattern.

stable state (−2.173 eV) when one C atom of the CO molecule bonds with two Co atoms from the substrate and one O atom bonds with one Zr atom (Fig. 5(e)). This is attributed to the non-uniform electron distribution in the gaseous CO molecule. The ICOHP of the C–O bond increases to −10.354, indicating a significant reduction in bond strength (Fig. 5(f–h)). This weakening primarily results from notable antibonding states within the energy range of −5 to 0 eV, caused by substantial charge interactions between the ZrCo substrate and the CO molecule.

To further evaluate the impact of V substitution on the hydrogen dissociation process, the energy barrier of the hydrogen dissociation in the presence of adsorbed CO on the ZrCo (110) surface (Fig. 5(m–o)) was determined. Remarkably, V substitution achieves a low barrier of 0.438 eV, in contrast to 0.618 eV for pristine ZrCo. As established, V atoms act as sacrificial sites that preferentially adsorb CO, thereby protecting numerous Co sites to serve as active centers for hydrogen dissociation. Concurrently, V doping further modulates the hydrogen dissociation activity and surface reactivity of the adjacent Co sites. This bifunctional synergy substantially enhances the CO poisoning resistance of the ZrCo-based alloy.

Cycling performance

Cycling stability during the de-/hydrogenation process represents another critical performance metric for assessing material applicability. As shown in Fig. 6(a and b), the cycling performance was evaluated in the presence of impurity gas. Specifically, the $ZrCo_{0.97}V_{0.03}$ alloy was hydrogenated under 4 bar H_2 + 5000 ppm CO and dehydrogenated under dynamic vacuum at 550 °C to avoid disproportionation.

As cycling proceeded, a gradual decrease in hydrogen capacity was observed in the ZrCoV alloy. The saturated capacity at the first cycle is 1.96 wt% and decreases to 1.57 wt% at the 25th cycle. Comparing the XRD patterns of the hydrogenated and dehydrogenated states before and after cycling (Fig. 6(c and d)), the Co_2C coating is *in situ* formed during the cycling process. Furthermore, XPS analysis of the surface valence state

of Co reveals the presence of both Co–C and metallic Co bonds (Fig. 6(e) and S9). However, in the $ZrCo_{0.97}V_{0.03}$ alloy, the low V content (3 at% substituting Co) results in a poor signal-to-noise ratio in the V 2p core-level spectrum (Fig. S10). This hinders reliable peak fitting and prevents definitive conclusions about the possible formation of VO_x or VC_x species. The strong adsorption of CO molecules likely promoted their direct reaction with the ZrCo alloy surface at elevated temperatures. Notably, no diffraction peaks corresponding to disproportionation products, such as the ZrH_2 or $ZrCo_2$ phase, can be observed in the XRD patterns. This confirms that Co_2C formed on the surface during cycling is the direct cause of capacity degradation. DFT calculations (Fig. S11) show that the formation energy of Co_2C is −0.92 eV, indicating a thermodynamic tendency for its formation. In contrast, after substituting part of the Co with V doping, the formation energy increases to 7.85 eV, which is unfavourable for this reaction. Therefore, V microalloying can effectively suppress the capacity decay caused by Co_2C formation during cycling.

Furthermore, SEM images and corresponding particle size distribution analyses before and after cycling are shown in Fig. S12(a–c). A clear reduction in the average particle diameter from 20 μm to 7.5 μm was observed, accompanied by the formation of numerous micro-cracks on the particle surfaces. The repeated lattice expansion and contraction caused by de-/hydrogenation lead to the micro-cracks and ultimately particle pulverization.[10,38–42] To further characterize the phase distribution, TEM analysis was performed on the after-cycle sample (Fig. 6(f–h)). FFT patterns taken from the near-surface region exhibited polycrystalline rings. The measured ring radius is 4.74 1/nm, corresponding to the (111) plane of the Co_2C phase (with a d-spacing of 0.211 nm). In contrast, FFT from the particle core matched the (110) plane of the B2-structured ZrCo-based matrix.[43–46] These results confirm the formation of a core–shell structure with a Co_2C-enriched surface layer. Since Co_2C lacks hydrogen absorption capacity, the inevitable formation of this phase in a CO-containing atmosphere results in irreversible capacity degradation during cycling. Nevertheless, this surface shell plays a critical role in notably enhancing both hydrogenation kinetics and CO poisoning resistance. Specifically, CO molecules exhibit unfavorable adsorption energy on the Co_2C surface, while the surface simultaneously facilitates efficient hydrogen dissociation. These combined characteristics enable the core–shell structure to improve hydrogenation activity in the presence of impurity gases.[17] Consequently, the Co_2C layer acts as a protective barrier that effectively shortens the hydrogenation time in the mixed impurity gas atmosphere.

Conclusions

In this work, we proposed a surface-hydrogenation activity factor as a descriptor for screening alloying modification elements to enhance the poisoning tolerance of ZrCo-based alloys. Computational screening results indicate that V exhibits both excellent hydrogen dissociation capability and a tendency to introduce positive strain. Combining theoretical and experimental analyses, V preferentially substitutes at the Co site. Among the investigated candidates, $ZrCo_{0.97}V_{0.03}$ alloy demonstrates a single-phase ZrCo structure and shows optimal overall performance. The incorporation of V induces localized positive strain in the ZrCo-based alloy and increases the surface potential, thereby promoting surface charge transfer and enhancing surface activity. Furthermore, V effectively reduces the hydrogen dissociation energy barrier under CO adsorption conditions. This multifunctional synergistic effect of V contributes to the significantly improved poisoning tolerance of the ZrCo-based alloy. Further cycling tests reveal that the $ZrCo_{0.97}V_{0.03}$ alloy maintains a capacity retention ratio of 80.1% after 25 cycles. This study provides advanced theoretical guidelines and a materials design strategy for enhancing the poisoning tolerance of hydrogen storage materials.

Author contributions

Qianwen Zhou: methodology, investigation, visualization, writing—original draft. Yiting Yu: methodology. Panpan Zhou: methodology, investigation, conceptualization, funding acquisition. Shunrui Xiao and Jingyu Hu: methodology. Xuezhang Xiao: conceptualization, funding acquisition. Xingwen Feng: methodology. Huaqin Kou: conceptualization, funding acquisition, methodology. Wenhua Luo: methodology. Xiulin Fan: methodology. Lixin Chen: conceptualization, methodology, funding acquisition, supervision, writing—review and editing. All authors took part in the discussion of data and gave comments on the manuscript.

Conflicts of interest

The authors declare no conflict of interest.

Data availability

The data supporting this article have been included as part of the supplementary information (SI). Supplementary information: experimental and theoretical details as well as additional characterization and performance data. See DOI: https://doi.org/10.1039/d6sc03342c.

Acknowledgements

This work is financially supported by the National MCF Energy R&D Program of China (2022YFE03170002), the National Natural Science Foundation of China (52071286, U2030208), and the Guangxi Science and Technology Major Project (no. AA24206007).

Notes and references

1 J. Kates-Harbeck, A. Svyatkovskiy and W. Tang, *Nature*, 2019, **568**, 526–531.
2 Y. Wu, Z. Chen, L. Hu, M. Jin, Y. Li, J. Jiang, J. Yu, C. Alejaldre, E. Stevens, K. Kim, D. Maisonnier, A. Kalashnikov, K. Tobita, D. Jackson and D. Perrault, *Nat. Energy*, 2016, **154**, 16154.

3 S. Le Pape, L. F. B. Hopkins, L. Divol, A. Pak, E. L. Dewald, S. Bhandarkar, L. R. Bennedetti, T. Bunn, J. Biener, J. Crippen, D. Casey, D. Edgell, D. N. Fittinghoff, M. Gatu-Johnson, C. Goyon, S. Haan, R. Hatarik, M. Havre, D. D. M. Ho, N. Izumi, J. Jaquez, S. F. Khan, G. A. Kyrala, T. Ma, A. J. Mackinnon, A. G. MacPhee, B. J. MacGowan, N. B. Meezan, J. Milovich, M. Millot, P. Michel, S. R. Nagel, A. Nikroo, P. Patel, J. Ralph, J. S. Ross, N. G. Rice, D. Strozzi, M. Stadermann, P. Volegov, C. Yeamans, C. Weber, C. Wild, D. Callahan and O. A. Hurricane, *Phys. Rev. Lett.*, 2018, **120**, 245003.

4 P. P. Zhou, Q. W. Zhou, X. Z. Xiao, X. L. Fan, Y. J. Zou, L. X. Sun, J. H. Jiang, D. Song and L. X. Chen, *Adv. Mater.*, 2025, **37**, 2413430.

5 H. Jiang, Z. Ding, Y. Li, G. Lin, S. Li, W. Du, Y. a. Chen, L. L. Shaw and F. Pan, *Chem. Sci.*, 2025, **16**, 7610–7636.

6 D. Zhang, X. Jia, H. B. Tran, S. H. Jang, L. Zhang, R. Sato, Y. Hashimoto, T. Sato, K. Konno, S.-i. Orimo and H. Li, *Chem. Sci.*, 2026, **17**, 3031–3042.

7 H. Kobayashi, M. Yamauchi, R. Ikeda, T. Yamamoto, S. Matsumura and H. Kitagawa, *Chem. Sci.*, 2018, **9**, 5536–5540.

8 M. Glugla, R. Lässer, L. Dörr, D. K. Murdoch, R. Haange and H. Yoshida, *Fusion Eng. Des.*, 2003, **69**, 39–43.

9 J. Roth, E. Tsitrone, T. Loarer, V. Philipps, S. Brezinsek, A. Loarte, G. F. Counsell, R. P. Doerner, K. Schmid, O. V. Ogorodnikova and R. A. Causey, *Plasma Phys. Controlled Fusion*, 2008, **50**, 103001.

10 P. Zhou, H. Shen, N. Xu, Q. Zhou, C. Yan, X. Li, N. Lei, J. Jiang, D. Song, J. Zheng, Y. Zou, L. Sun, Z. Han, X. Fan, X. Xiao and L. Chen, *Energy Storage Mater.*, 2026, **84**, 104789.

11 Z. Y. Li, S. Y. Liu, Y. H. Pu, G. Huang, Y. B. Yuan, R. Q. Zhu, X. F. Li, C. Y. Chen, G. Deng, H. H. Zou, P. Yi, M. Fang, X. Sun, J. Z. He, H. Cai, J. X. Shang, X. F. Liu, R. H. Yu and J. L. Shui, *Nat. Commun.*, 2023, **14**, 7966.

12 R. D. Penzhorn, M. Devillers and M. Sirch, *J. Nucl. Mater.*, 1990, **170**, 217–231.

13 G. Federici, C. H. Skinner, J. N. Brooks, J. P. Coad, C. Grisolia, A. A. Haasz, A. Hassanein, V. Philipps, C. S. Pitcher, J. Roth, W. R. Wampler and D. G. Whyte, *Nucl. Fusion*, 2001, **41**, 1967–2137.

14 J. P. Bi, P. P. Zhou, W. Jiang, H. Q. Kou, T. Tang, Y. J. Zhang, Y. Liu, Q. W. Zhou, Y. X. Yao, Y. Zhang, M. Yang, L. X. Chen and X. Z. Xiao, *Adv. Sci.*, 2024, **11**, 2408522.

15 J. P. Bi, P. P. Zhou, X. Z. Xiao, Y. J. Zhang, H. Q. Kou, T. Tang and L. X. Chen, *Chem. Eng. J.*, 2024, **481**, 148517.

16 Y. Shang, A. Santhosh, M. Ante, L. Wimbert, P. Jerabek, T. Schupp, T. Klassen and C. Pistidda, *Acta Mater.*, 2025, **298**, 121398.

17 Q. Zhou, P. Zhou, J. Bi, L. Zhang, S. Xiao, X. Xiao, X. Fan and L. Chen, *J. Energy Chem.*, 2025, **108**, 254–262.

18 D. J. Long, Y. D. Liu, X. Y. Ping, F. D. Chen, X. X. Tao, Z. Y. Xie, M. J. Wang, M. Wang, L. Li, L. Guo, S. G. Chen and Z. D. Wei, *Nat. Commun.*, 2024, **15**, 8105.

19 G. Blyholder, *J. Phys. Chem.*, 1964, **68**, 2772–2777.

20 J. Prigent, M. Latroche, E. Leoni and V. Rohr, *J. Alloys Compd.*, 2011, **509**, S801–S803.

21 P. Zhou, J. Bi, Q. Zhou, N. Lei, H. Shen, J. Jiang, D. Song, X. Xiao and L. Chen, *J. Energy Storage*, 2026, **141**, 119285.

22 H. Shi, W.-G. Cui, Z. Li, F. Gao, X. Wang, K. Wang, Y. Gao, Y. Yang, Z. Shen, Y. Liu, J. Miao, X. Xiao, F. Fang and H. Pan, *Energy Technol.*, 2025, **13**, 2500132.

23 Y. J. Zhang, P. P. Zhou, X. Z. Xiao, J. P. Bi, X. Y. Zhang, H. Q. Kou, X. Huang, T. Tang and L. X. Chen, *Chem. Eng. J.*, 2024, **479**, 147660.

24 X. M. Guo, S. M. Wang, Z. N. Li, B. L. Yuan, J. H. Ye, H. C. Qiu, Y. F. Wu, X. P. Liu and L. J. Jiang, *Fusion Eng. Des.*, 2016, **113**, 195–200.

25 H. L. Li, S. M. Wang, L. J. Jiang, L. D. Zhang, X. P. Liu and Z. N. Li, *Rare Met.*, 2008, **27**, 367–370.

26 G. H. Zhang, T. Tang, G. Sang, Y. F. Xiong, H. Q. Kou, W. Q. Wu and Y. J. Wei, *Rare Metal Mat. Eng.*, 2017, **46**, 3366–3373.

27 J. Gu, Z. Yao, J. Zhang, M. Liu, W. Li, H. Wang, Z. Huang, J. Xie, G. Gao, M. Chen, C. Li, M. Fan, X. Xiao and L. Chen, *Int. J. Hydrogen Energy*, 2024, **88**, 69–77.

28 Z. Liang, X. Xiao, J. Qi, H. Kou and L. Chen, *J. Alloys Compd.*, 2023, **932**, 167552.

29 Z. Q. Hou, C. H. Cui, Y. N. Li, Y. J. Gao, D. M. Zhu, Y. F. Gu, G. Y. Pan, Y. Q. Zhu and T. Zhang, *Adv. Mater.*, 2023, **35**, 2209876.

30 C. Chen, Y. J. Kang, Z. Y. Huo, Z. W. Zhu, W. Y. Huang, H. L. L. Xin, J. D. Snyder, D. G. Li, J. A. Herron, M. Mavrikakis, M. F. Chi, K. L. More, Y. D. Li, N. M. Markovic, G. A. Somorjai, P. D. Yang and V. R. Stamenkovic, *Science*, 2014, **343**, 1339–1343.

31 Q. W. Zhou, P. P. Zhou, J. P. Bi, L. C. Zhang, S. R. Xiao, X. Z. Xiao, X. L. Fan and L. X. Chen, *J. Energy Chem.*, 2025, **108**, 254–262.

32 B. Zhang, B. Luo, G. Sang, H. Kou, P. Li and W. Luo, *Int. J. Hydrogen Energy*, 2026, **219**, 154103.

33 B. Zhang, B. Luo, W. Luo, L. Zhou, H. Kou, P. Li and G. Sang, *Int. J. Hydrogen Energy*, 2024, **86**, 899–912.

34 M. Bououdina, B. Lambert-Andron, B. Ouladdiaf, S. Pairis and D. Fruchart, *J. Alloys Compd.*, 2003, **356**, 54–58.

35 D. Shaltiel, I. Jacob and D. Davidov, *J. Less-Common Met.*, 1977, **53**, 117–131.

36 Q. L. Liang, J. Y. Wang, D. Wang, X. D. Ding, Y. Z. Wang and M. J. Mills, *Acta Mater.*, 2025, **284**, 120629.

37 Q. Q. Zhang, H. Shen, Y. Yang, Y. N. Liu, Y. T. Liu, Z. H. Zhang, L. S. Cui and S. J. Hao, *J. Alloys Compd.*, 2025, **1013**, 178450.

38 P. Zhou, Q. Zhou, W. Liu, N. Lei, Y. Chen, J. Jiang, D. Song, H.-W. Li, Q.-Y. Li, L. Chen and X. Xiao, *Adv. Sci.*, 2025, **12**, e13463.

39 J. Tu, P. Zhou, S. Chen, S. Shen, X. Liu, X. Xiao, Z. Li and L. Ouyang, *Mater. Sci. Eng. R Rep.*, 2026, **167**, 101089.

40 P. P. Zhou, X. Z. Xiao, X. Y. Zhu, Y. P. Chen, W. M. Lu, M. Y. Piao, Z. M. Cao, M. Lu, F. Fang, Z. N. Li, L. J. Jiang and L. X. Chen, *Energy Storage Mater.*, 2023, **63**, 102964.

41 J. Bi, P. Zhou, Q. Zhou, Y. Liu, L. Tang, S. Xiao, N. Lei, F. Chu, H. Kou, T. Tang, L. Chen and X. Xiao, *Renewable Energy*, 2026, **256**, 124226.

42 P. P. Zhou, Z. M. Cao, X. Z. Xiao, L. J. Zhan, J. H. He, Y. Y. Zhao, L. Wang, M. Yan, Z. N. Li and L. X. Chen, *Mater. Today Energy*, 2023, **33**, 101258.
43 J. Qi, X. Zhang, B. Yu, X. Xiao, F. Chu, T. Ying, X. Feng, J. Song, Y. Shi, H. Kou, C. Chen, W. Luo and L. Chen, *Energy Environ. Mater.*, 2025, **8**, e70000.
44 Z. Yao, X. Xiao, Z. Liang, X. Huang, H. Kou, W. Luo, C. Chen and L. Chen, *J. Mater. Chem. A*, 2020, **8**, 9322–9330.
45 Z. Yang, Y. Jia, Y. Liu, F. Chu, J. Qi, T. Ying, J. He, X. Feng, J. Song, Y. Shi, W. Luo, X. Xiao and L. Chen, *Adv. Sci.*, 2025, **12**, e07722.
46 Z. Yang, Y. Jia, Y. Liu, X. Xiao, T. Ying, X. Feng, Y. Shi, C. Chen, W. Luo and L. Chen, *Energy Mater.*, 2025, **5**, 500011.